

1    **Supporting Information for**

2    **“Joint inversion of co-seismic and early post-seismic slip to optimize the in-**  
 3    **formation content in geodetic data: Application to the 2009 M<sub>w</sub>6.3 L’Aquila**  
 4    **earthquake, Central Italy”**

5    **Théa Ragon<sup>1</sup>, Anthony Sladen<sup>1</sup>, Quentin Bletry<sup>1</sup>, Mathilde Vergnolle<sup>1</sup>, Olivier Cavalié<sup>1</sup>,**  
 6    **Antonio Avallone<sup>2</sup>, Julien Balestra<sup>1</sup>, Bertrand Delouis<sup>1</sup>**

7    <sup>1</sup>Université Côte d’Azur, CNRS, Observatoire de la Côte d’Azur, IRD, Géoazur, Valbonne, France

8    <sup>2</sup>Istituto Nazionale di Geofisica e Vulcanologia, Rome, Italy

9    **Contents**

- 10    1. Text S1
- 11    2. Tables S1 to S2
- 12    3. Figures S1 to S14

13    **Text S1. Description of the observations**

14    The strictly co-seismic dataset contains static offsets analyzed from the 31 1 Hz-sampled and  
 15    the two 10 Hz-sampled high rate GPS stations located in the earthquake area. Strictly co-seismic  
 16    offsets have been calculated from the difference on the 3 components between mean position before  
 17    the event ( $[t_0-5 \text{ s} : t_0]$ ) and after the event ( $[t_0+25 \text{ s} : t_0+30 \text{ s}]$ ) [Avallone *et al.*, 2011]. Data errors  
 18    are used to build a diagonal covariance matrix  $\mathbf{C}_d^{\text{gps}}$  describing observational uncertainties.

19    The 6 days of co and early post-seismic dataset contains 40 static GPS offsets and 2 InSAR  
 20    frames. We consider the continuous GPS sites included in Cheloni *et al.* [2010] and 2 survey style  
 21    GPS sites. Offsets have been calculated from the difference on the 3 components between mean  
 22    position before the event and 6 days after the event. Mean values and relative uncertainties have  
 23    been calculated for a time interval of 7 days before  $t_0$  and on the period between 5 and 7 days after  
 24     $t_0$ . This approach mirrors the high rate GPS analysis [Avallone *et al.*, 2011] and allows to calculate  
 25    reliable uncertainties on the 3 days period around the 6th day after earthquake. Uncertainties are  
 26    added to the observational errors matrix  $\mathbf{C}_d^{\text{gps}}$ . Additionally, two post-seismic COSMO-SkyMed  
 27    and ENVISAT images have been acquired the October 12th 2009, 6 days after the mainshock. Two  
 28    differential interferograms have thus been generated, each containing co-seismic displacement and 6  
 29    days of post-seismic signal: an ascending COSMO-SkyMed frame and a descending Envisat frame  
 30    (Tab. S1). The interferograms have been processed using the JPL/Caltech ROI\_PAC software [Rosen  
 31    *et al.*, 2004]. To improve computational efficiency, we resample InSAR observations based on model  
 32    resolution [Lohman and Simons, 2005] with windows ranging from 12 km to 1 km. We account  
 33    for measurement uncertainties by building a data covariance matrix. To do so, we mask the area  
 34    of coseismic displacement and estimate empirical covariograms as a function of distance between  
 35    data points (Figure S2). Then, the InSAR covariance matrix  $\mathbf{C}_d^{\text{insar}}$  is calculated from the best fitting  
 36    exponential function to empirical covariograms [Jolivet *et al.*, 2012].

---

Corresponding author: Théa Ragon, ragon@geoazur.unice.fr

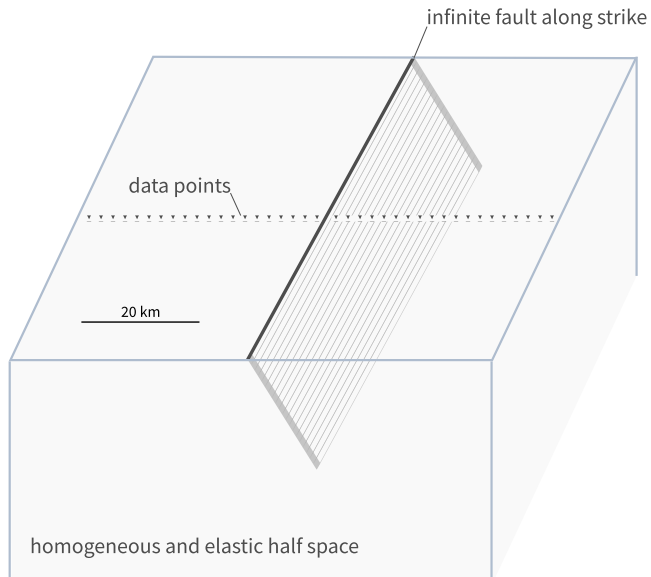
37 **Supplementary Tables**

Satellite (orbit pass)	Interferogram pair	Mean incidence angle
COSMO-SkyMed (ascending)	04/04/2009 - 12/04/2009	35.9
Envisat (descending)	24/04/2008 - 12/04/2009	23

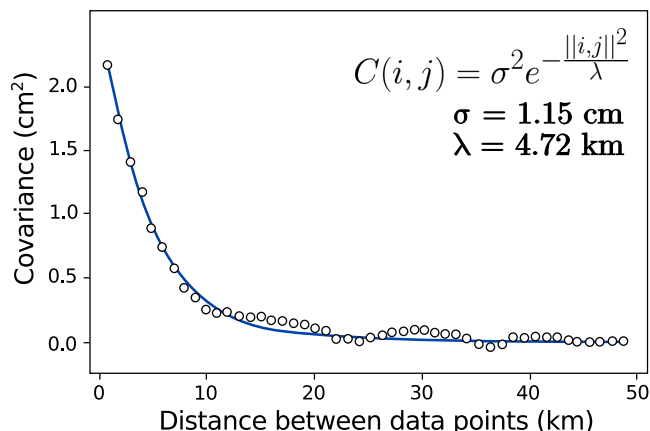
38 **Table S1.** Interferometric pairs used in this study.

	CTW approach, with $\mathbf{C}_p$ COpref and POSTpref	CTW approach, no $\mathbf{C}_p$ sCO and sPOST	Strictly Coseismic, no $\mathbf{C}_p$ COgps	Co+post-seismic no $\mathbf{C}_p$ CO+POST
<b>GPS, co-seismic</b>	1.19	1.14	1.13	1.43
<b>GPS, 6 days offset</b>	0.899	0.697	1.22	0.826
<b>COSMO-SkyMed asc.</b>	4.11	3.98	8.82	3.96
<b>Envisat dsc.</b>	1.76	2.02	10.1	1.88

39 **Table S2.** Residuals between observations and predictions (RMS in centimetre) for slip models inferred within  
40 the CTW approach, accounting or not for  $\mathbf{C}_p$ , and for slip models inferred independently: strictly co-seismic  
41 slip model and co and post-seismic slip model, without accounting for  $\mathbf{C}_p$ .

42  
**Supplementary Figures**

43 **Figure S1.** Schematic view of the 2D simplified toy model we use to explore the impact of the CTW approach  
 44 on the inferred models. The assumed fault extends infinitely along strike, but is discretized into 20 subfaults of 1  
 45 km width. The synthetic data are distributed along a profile line perpendicular to the fault strike, centred on the  
 46 fault at the surface. There are 100 data points that are spaced every kilometer. The medium is a homogeneous  
 47 and elastic half space.



48 **Figure S2.** Empirical covariance functions for the Envisat descending interferogram. One dimensional  
 49 empirical covariance functions and associated best fit exponential functions for the displacements derived from  
 50 InSAR data. For each interferogram, we compute the empirical covariance as a function of the inter-pixel  
 51 distance and then fit an exponential function (Jolivet et al. 2012). The exponential function is used to build the  
 52 data covariance matrix.

**Median model of the 25 families of models**

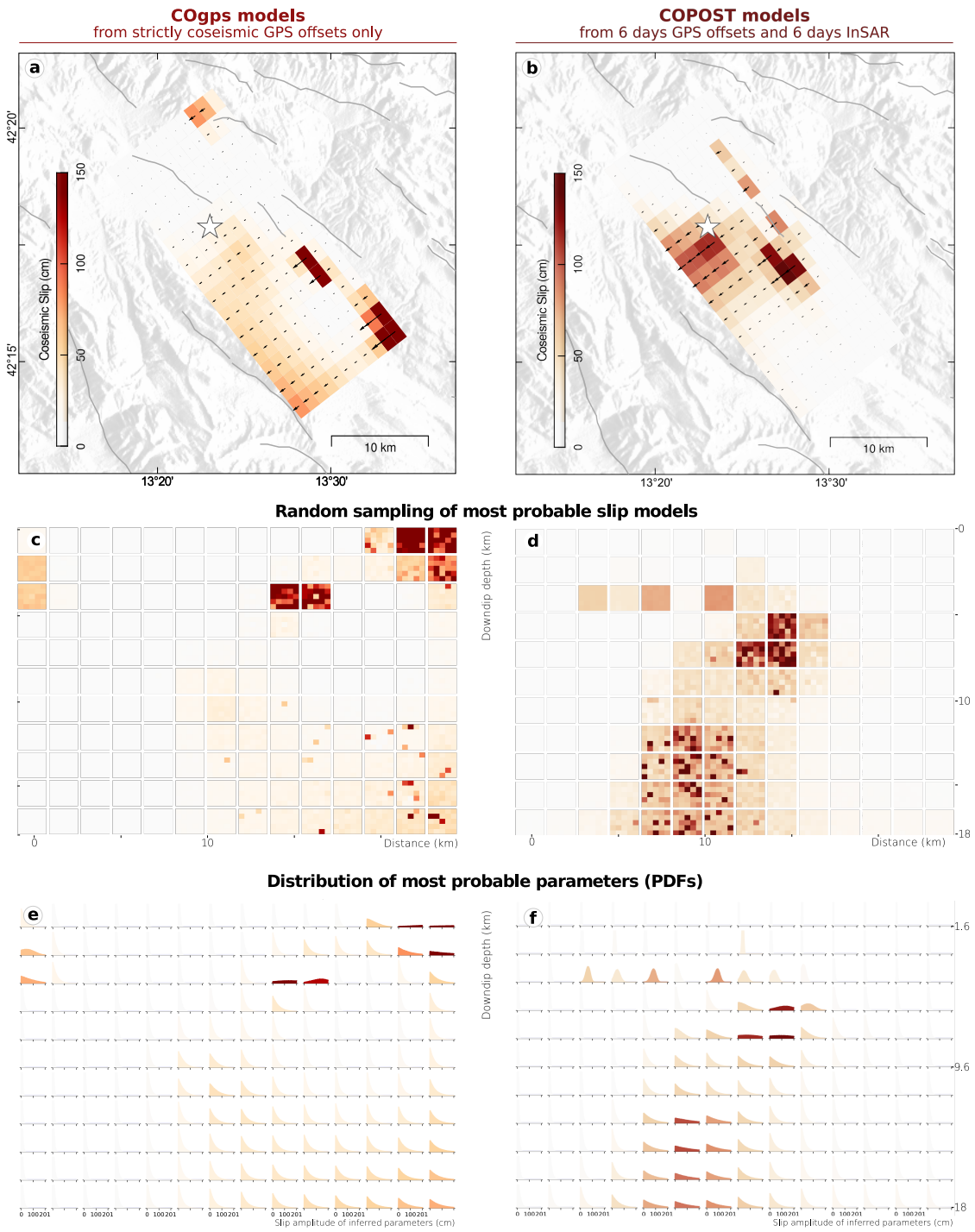
Each parameter of the models included in this family are less than 50cm from the median sample parameters

If one sample selected randomly does not belong to the previous families, it becomes the master of another family

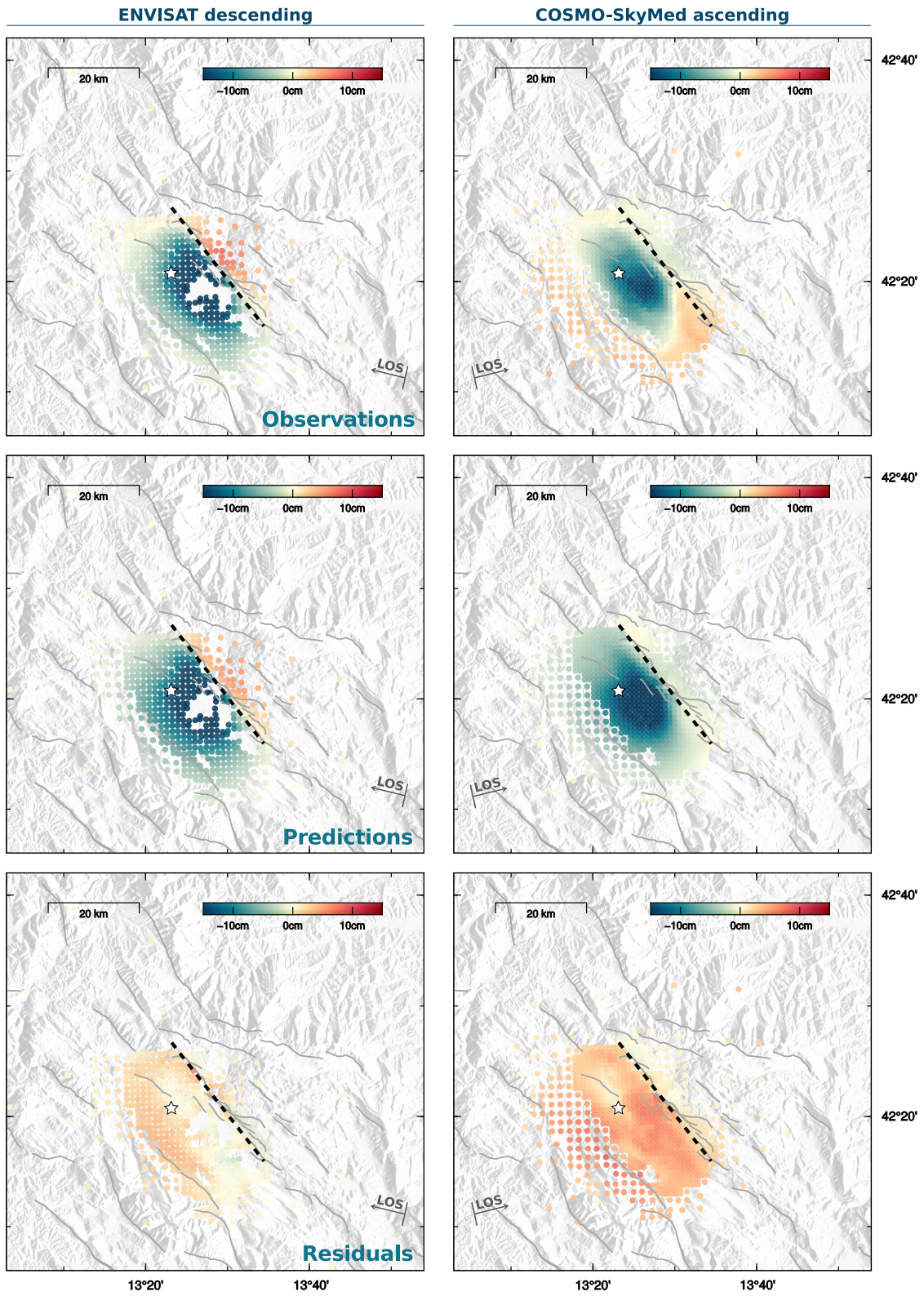
**One random sample selected among the samples of the 25 families of models**

53 **Figure S3.** The set of samples inferred from an inversion is divided into 25 families. The first family gathers  
 54 samples whose parameters deviate of less than 50 cm from the median model parameters (for the co-seismic  
 55 slip). In detail, a model is added to the first family if the selected model and the median model are parameter-  
 56 wise equal within a tolerance of 50 cm for the co-seismic slip, and a tolerance of 25 cm for the post-seismic  
 57 slip. Other families are built iteratively around a randomly selected model that has not fitted within antecedent  
 58 families, except for the last family which gathers orphan samples. (continued)

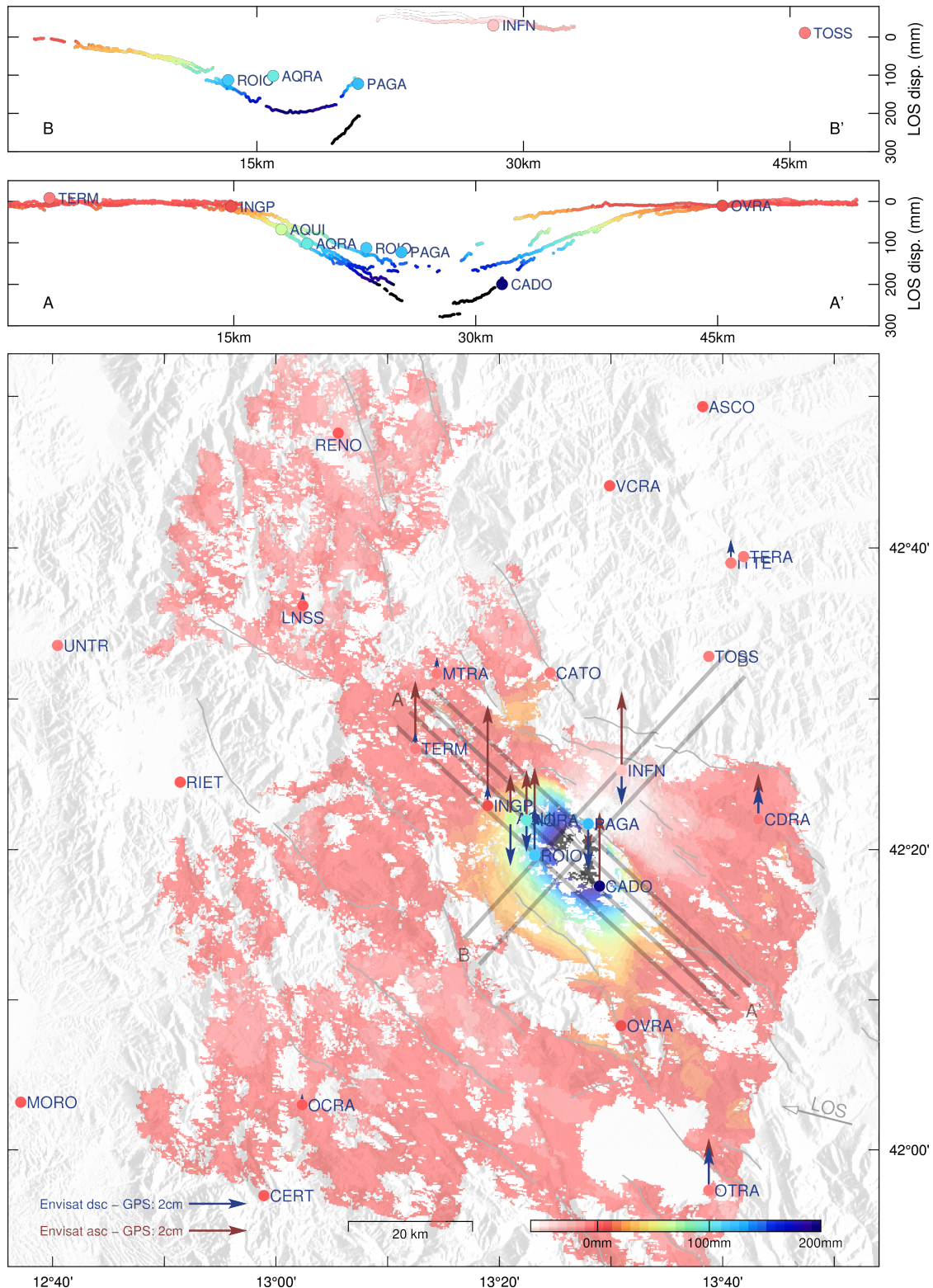
59      **Figure S3.** (Previous page.) In (a), the median model of each family is shown for the co-seismic slip model  
60      inferred accounting for  $\mathbf{C}_p$  with the CTW approach. In (b), one sample is selected randomly in each of the 25  
61      subsets. Figures 3a-d and 5a-b illustrate the median parameters of the 25 families of (a) for each subfault: for  
62      instance, the top right pixels of each subfault in Figure 5a correspond to the parameters of the median model of  
63      the first family shown in (a).



64 **Figure S4.** Finite-fault slip models inferred from strictly co-seismic data (model COgps) or data including  
 65 the co-seismic phase plus some early post-seismic deformation (model COPOST). (a) and (b) show the slip  
 66 amplitude and rake of the median model, the epicenter being the white star. The color scale is the same for all  
 67 the figures. (c) and (d) illustrate the slip amplitude of the median models of 25 families of inferred models (more  
 68 information in the text and Figure S4). This presentation allows a visual estimation of the covariance between  
 69 probable models at the scale of subfaults. (e) and (f) represent the posterior probability density functions of the  
 70 300000 samples for each model parameter, and thus the amount of samples that have inferred slip values for  
 71 each subfault. The PDFs are colored from the median model, the color-scale being the same as in (a) and (b)  
 72 respectively.



73 **Figure S5.** Fit to the InSAR dataset for the median COPOST model. Observations, predictions inferred  
 74 from the average model and residuals are shown for ENVISAT descending and COSMO-SkyMed ascending  
 75 interferograms, respectively to the left and to the right. The assumed fault trace is shown with a dotted black  
 76 line. The epicenter is the white star. Seismogenic faults are shown in light gray.



77 **Figure S6.** Comparison between co+post GPS and InSAR datasets. The ENVISAT interferogram is shown in  
 78 background. GPS offsets between mainshock and 6 days after in the Line of Sight (LOS) direction are shown in  
 79 colored dots in the same colorscale. The offset between surface displacement in the LOS direction of ENVISAT  
 80 interferogram and GPS is shown with dark blue arrows. Four NW-SE profiles (A - A') and two SW-NE profiles  
 81 (B - B') represent the LOS displacement of InSAR points along these profiles and of adjacent GPS stations.

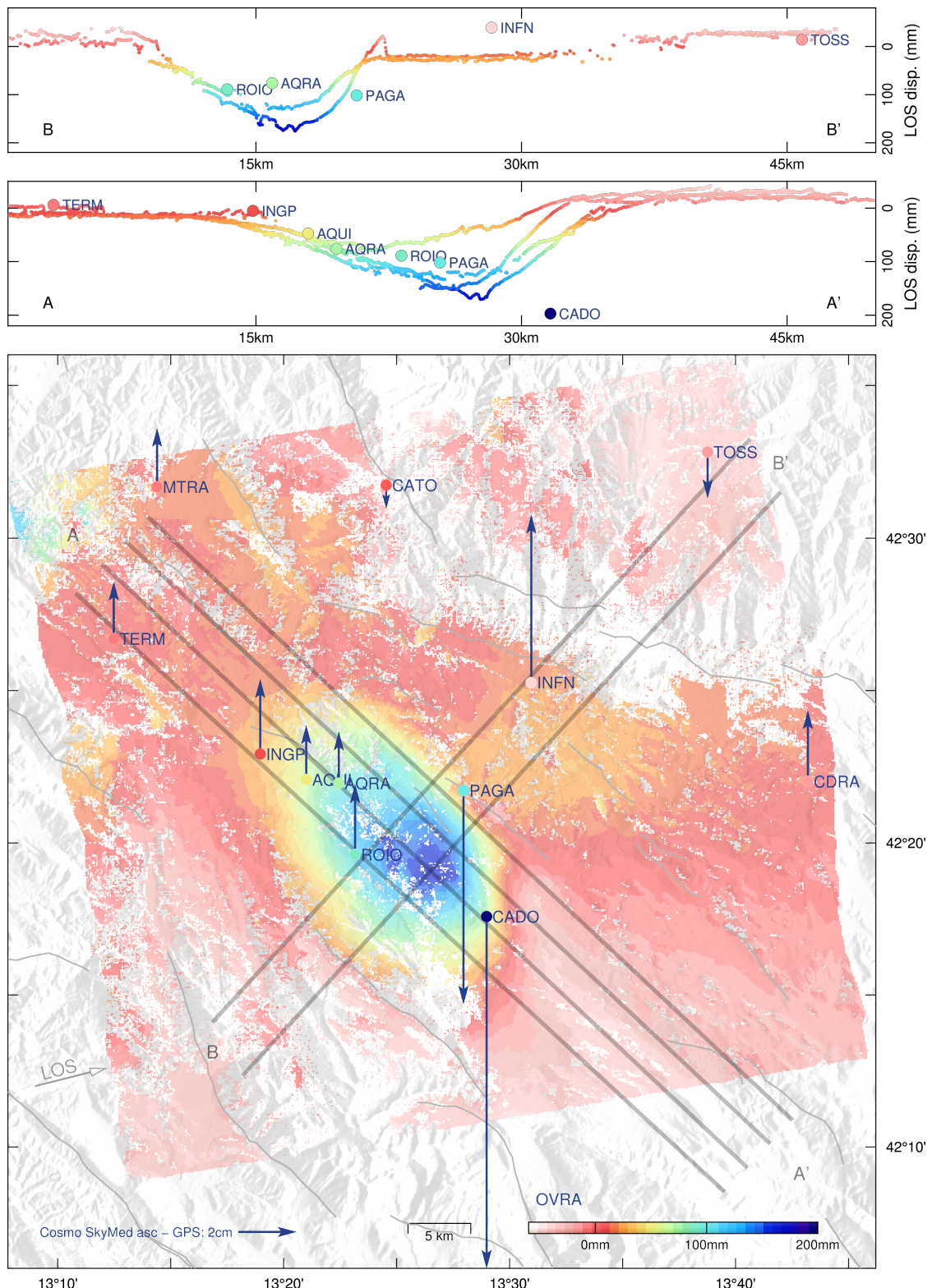
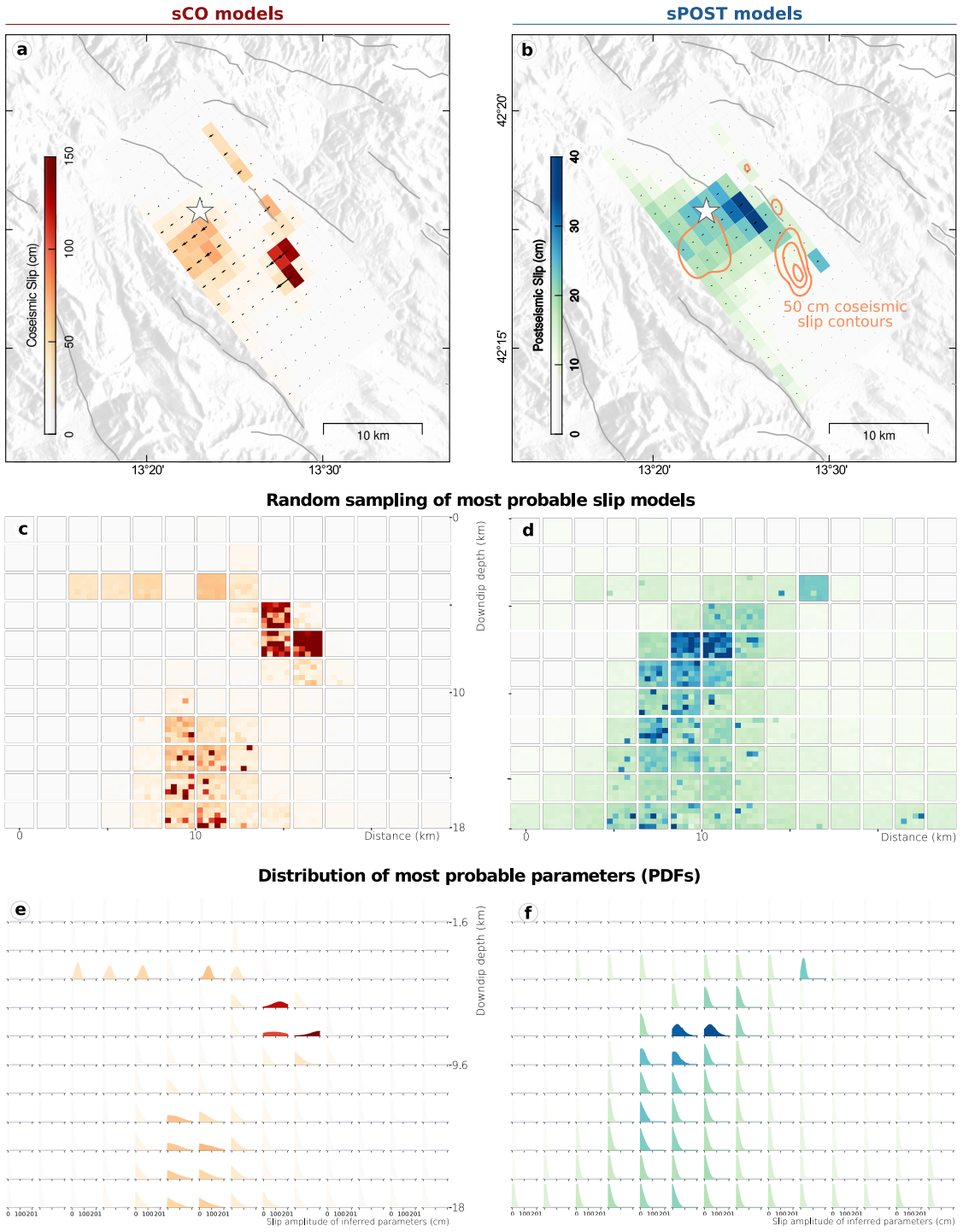


**Figure S7.** Comparison between co+post GPS and InSAR datasets. The COSMO-SkyMed interferogram is shown in background. GPS offsets between mainshock and 6 days after in the Line of Sight (LOS) direction are shown in colored dots in the same colorscale. The offset between surface displacement in the LOS direction of COSMO-SkyMed interferogram and GPS is shown with dark blue arrows. Four NW-SE profiles (A - A') and two SW-NE profiles (B - B') represent the LOS displacement of InSAR points along these profiles and of adjacent GPS stations.

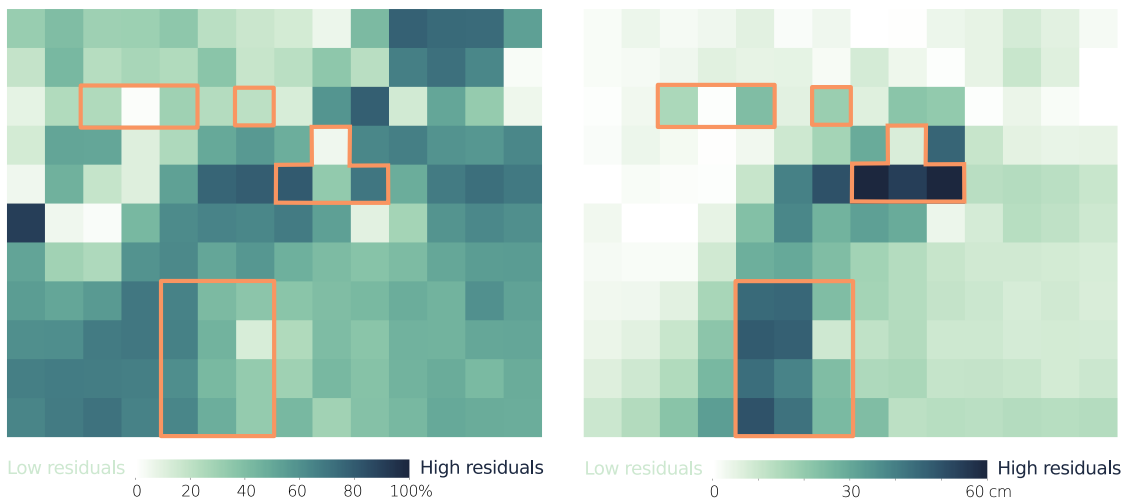


88 **Figure S8.** Strictly co-seismic (model sCO) and early postseismic (model sPOST) finite fault slip models,  
 89 inferred with the CTW approach and without accounting for epistemic uncertainties. (a) and (b) show the slip  
 90 amplitude and rake of the median model, the epicenter being the white star. In (b), orange lines also show the  
 91 50 cm coseismic slip contours. The color scale is the same for all the figures. (c) and (d) illustrate the slip  
 92 amplitude of the median models of 25 families of inferred models. (e) and (f) represent the posterior probability  
 93 density functions of the 300000 samples for each model parameter. The PDFs are colored from the median  
 94 model, the color-scale being the same as in (a) and (b) respectively.

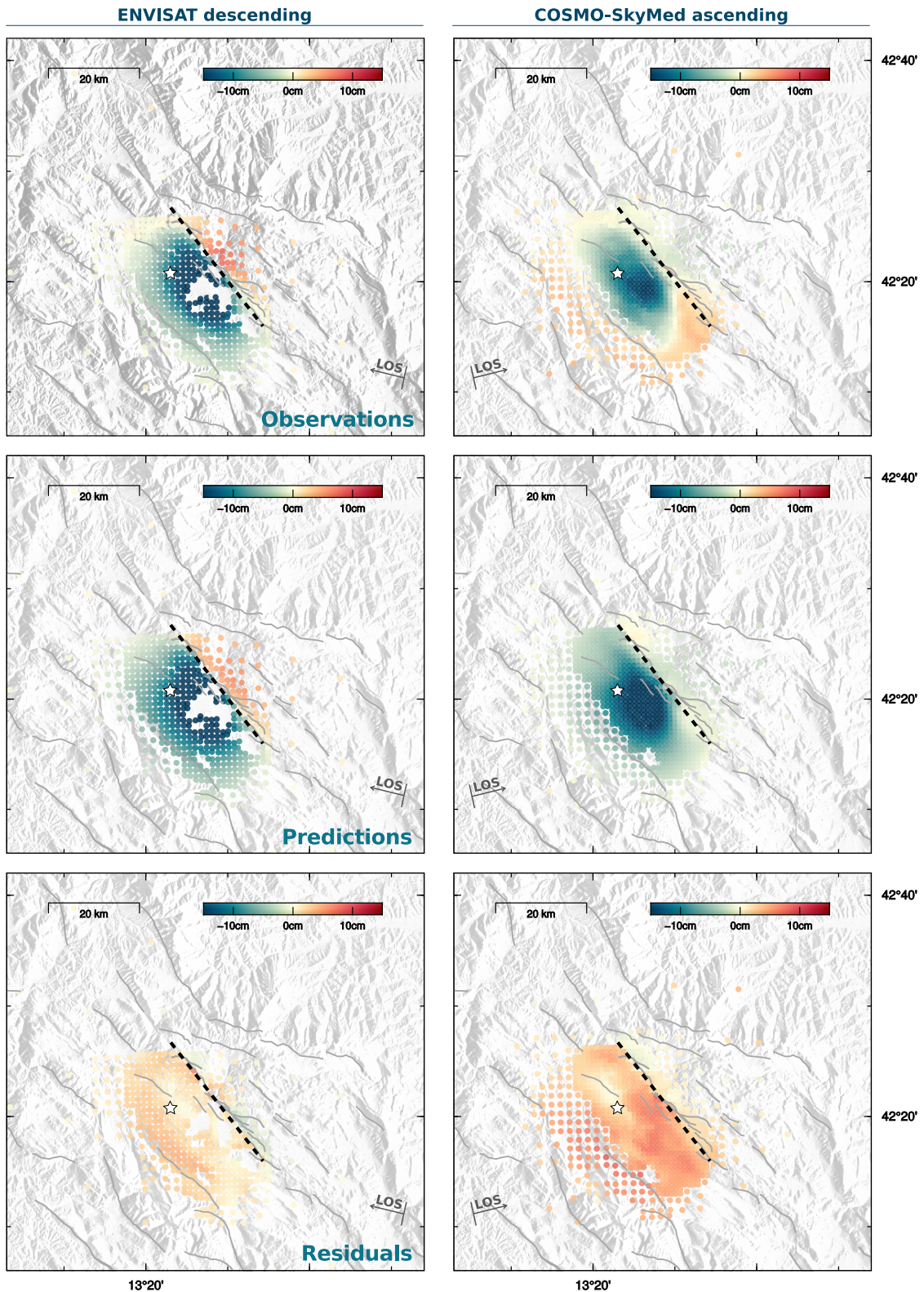


95 **Figure S9.** Animated slip distribution of the model sCO. We divide our 300000 most probable models into  
 96 25 families of models. We then select randomly a sample of each family: the parameters of each sample are  
 97 depicted by colored pixels in corresponding subfaults for the first step of the animation. Another random set of  
 98 25 samples is selected and represented in the second step of the animation, and so forth.

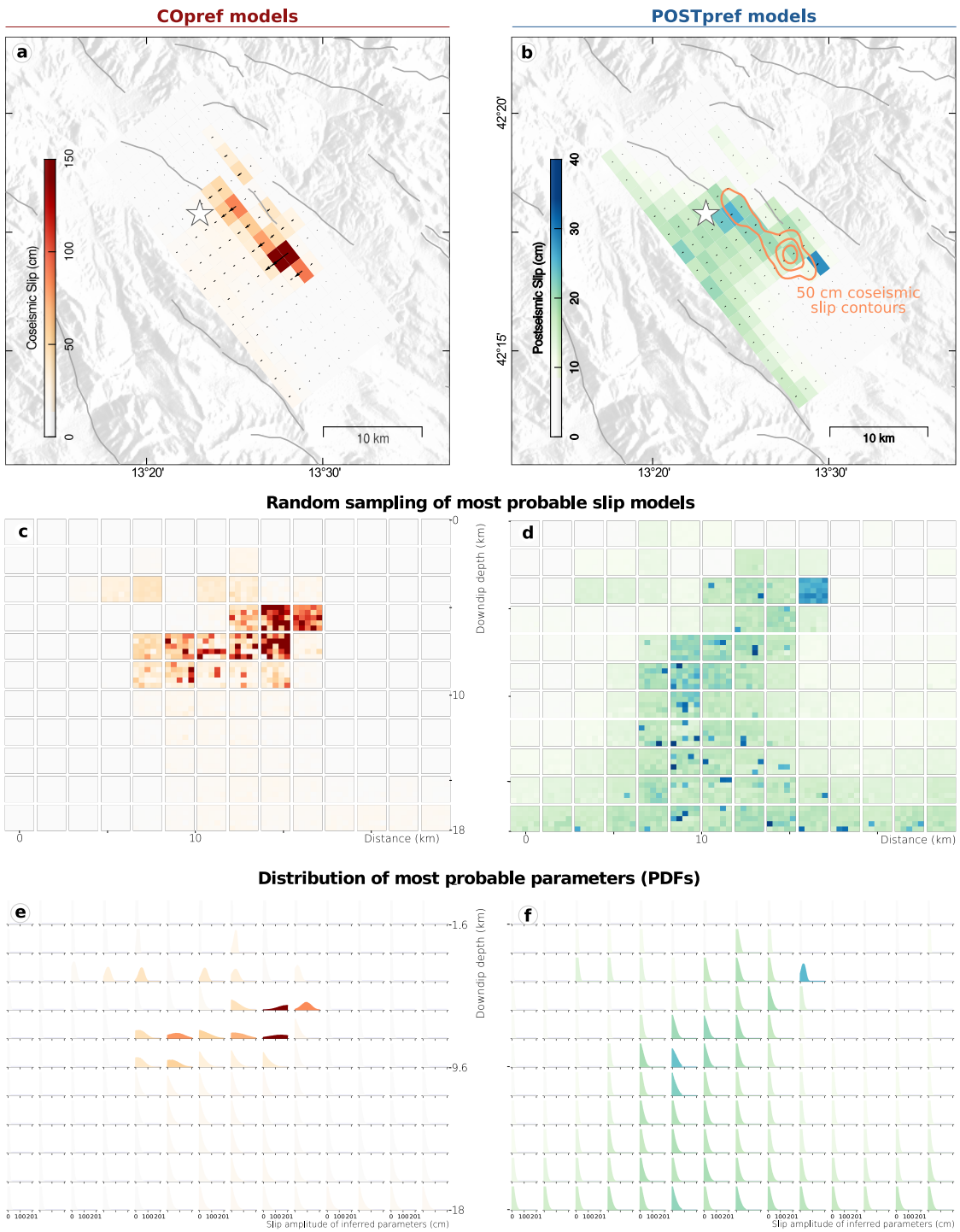
99 To launch the animation, click on the image. The animation will display in Acrobat Reader preferably. If  
 100 not displayed, you can find the same animation at the following address: <https://ragonthea.wordpress.com/re->  
 101 [search/fault\\_geom/](https://ragonthea.wordpress.com/research/fault_geom/)



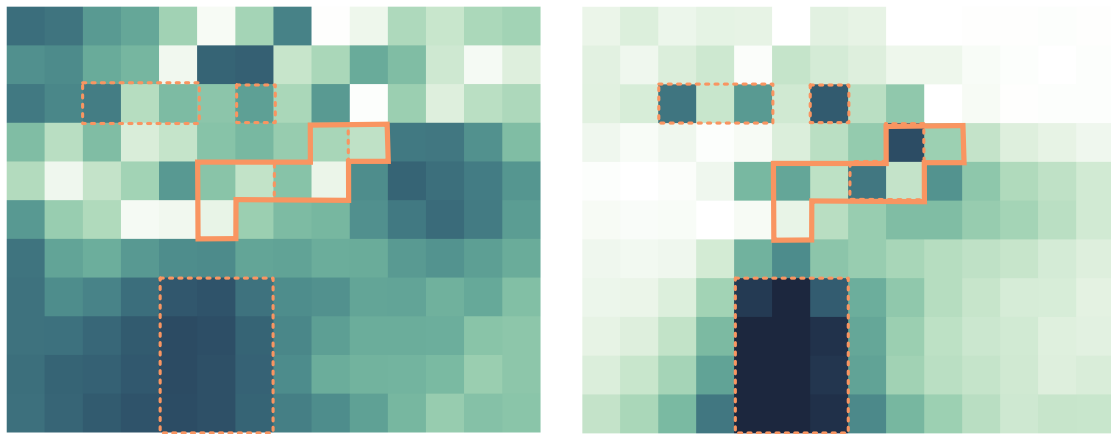
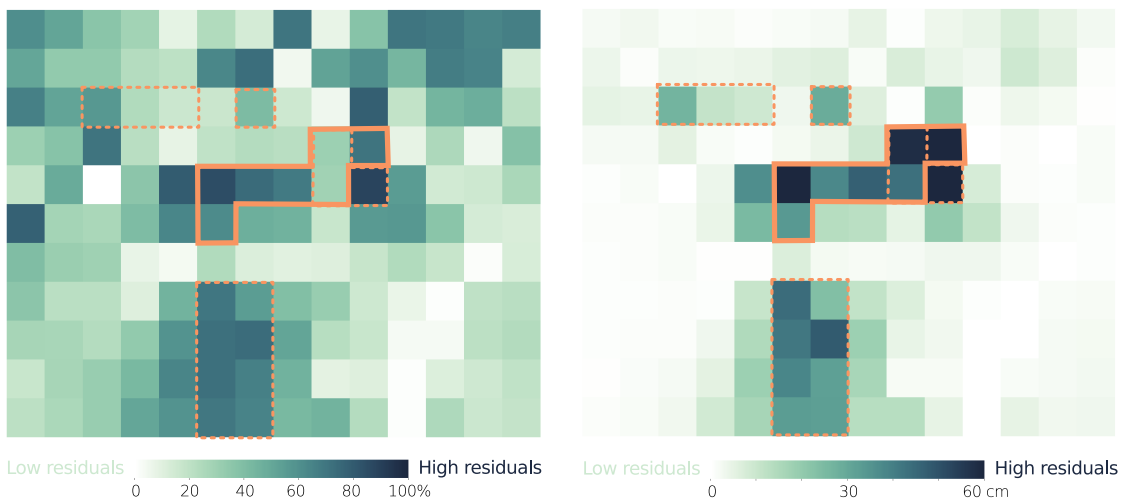
102 **Figure S10.** Comparison between the median models sCO and COPOST. Left, the residuals in percentage of  
 103 slip amplitude for each subfault are shown. Right, the residuals in cm are shown. The orange lines delimit the  
 104 area in which slip amplitude is greater than 60 cm.



105 **Figure S11.** Fit to the InSAR dataset for the median models sCO and sPOST. Observations, predictions  
 106 inferred from the average model and residuals are shown for ENVISAT descending and COSMO-SkyMed  
 107 ascending interferograms, respectively to the left and to the right. The assumed fault trace is shown with a  
 108 dotted black line. The epicenter is the white star. Seismogenic faults are shown in light gray.



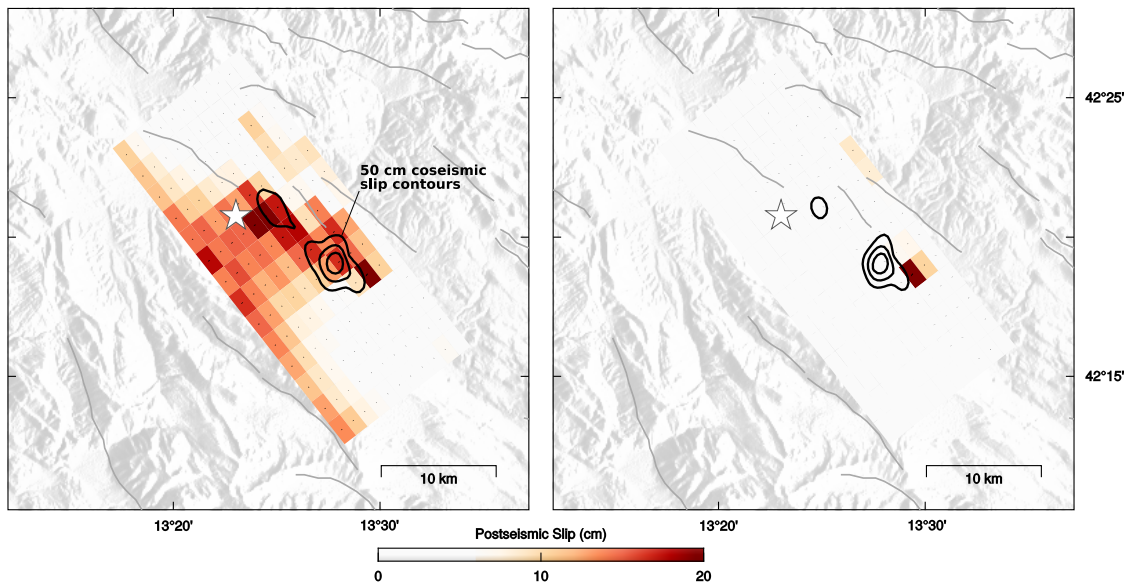
109 **Figure S12.** Our preferred models COpref and POSTpref, inferred with the CTW approach and accounting  
 110 for epistemic uncertainties. (a) and (b) show the slip amplitude and rake of the average model, the epicenter  
 111 being the white star. In (b), orange lines also show the 50 cm co-seismic slip contours. The color scale is the  
 112 same for figures a,c,e and b,d,f. (c) and (d) illustrate the slip amplitude of the median models of 25 families  
 113 of inferred models. (e) and (f) represent the posterior probability density functions of the 300000 samples for  
 114 each parameter, and thus the amount of samples that have inferred slip values for each subfault. The PDFs are  
 115 colored from the median model, the color-scale being the same as in (a) and (b) respectively.

Residuals between **COpref** and **COPOST** median modelsResiduals between **COpref** and **sCO** median models

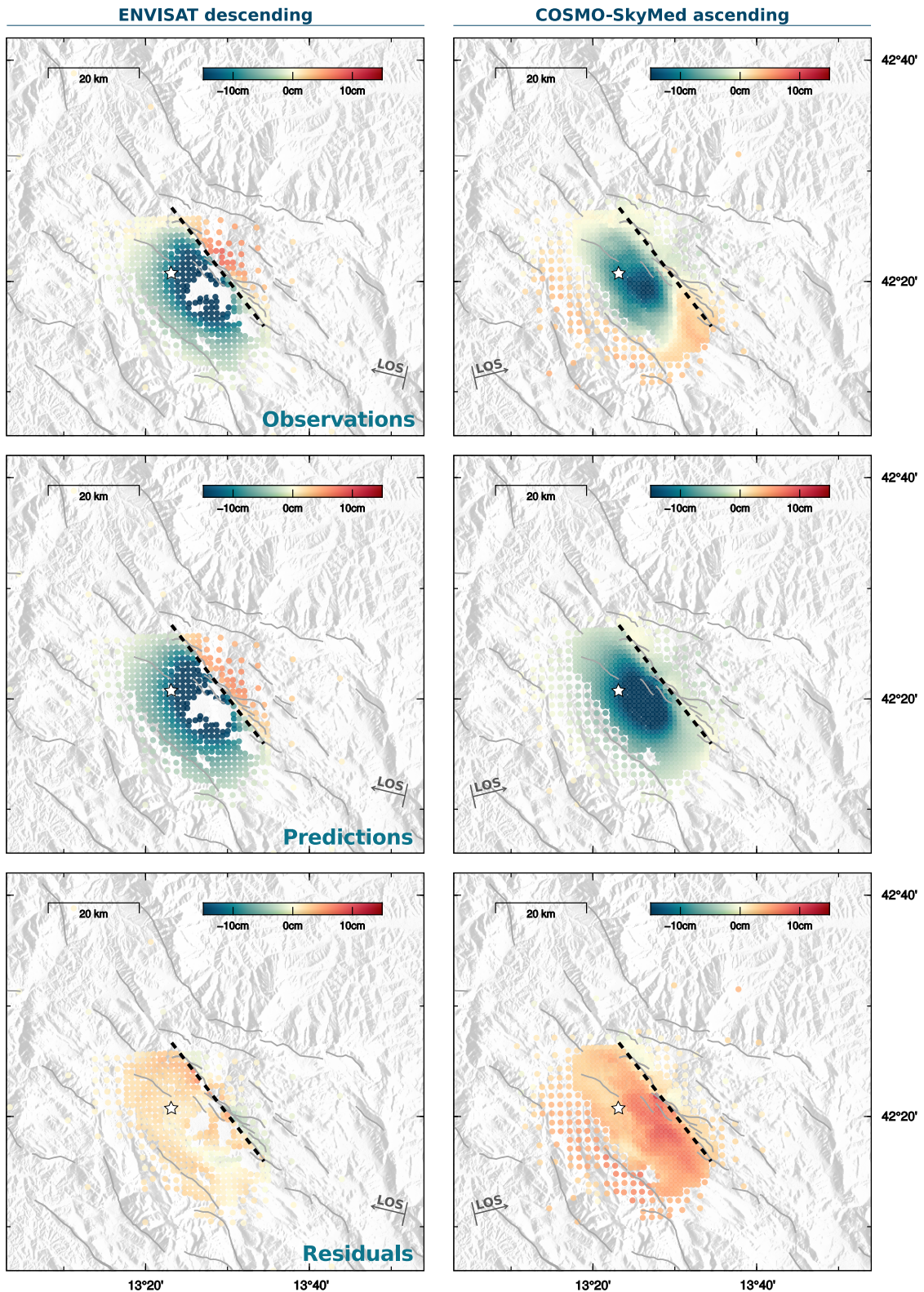
116 **Figure S13.** Comparison between our median model COpref and COPOST (top) or sCO (bottom). Left, the  
 117 residuals in percentage of slip amplitude for each subfault are shown. Right, the residuals in cm are shown. The  
 118 orange lines delimit the area in which the slip amplitudes of model COpref exceed 50 cm. The dotted orange  
 119 line delimit these area for model COPOST (top) or model COpref (bottom). The residuals with the COPOST  
 120 model (top) are largest for the deepest parts of the fault, reaching 90%. The residuals with the sCO model  
 121 (bottom) exceed 60% for high slip area.



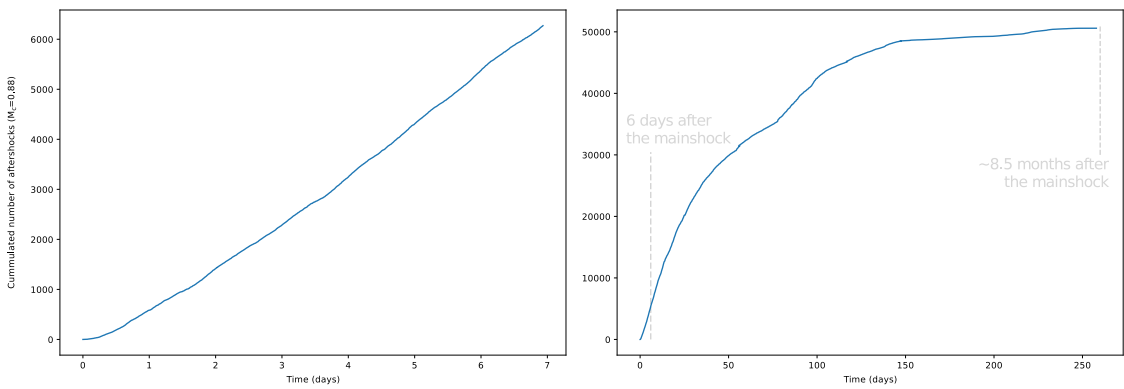
122 **Figure S14.** Animated slip distribution of the COpref model. We divide our 300000 most probable models  
 123 into 25 families of models. We then select randomly a sample of each family: the parameters of each sample  
 124 are depicted by colored pixels in corresponding subfaults for the first step of the animation. Another random  
 125 set of 25 samples is selected and represented in the second step of the animation, and so forth.  
 126 To launch the animation, click on the image. The animation will display in Acrobat Reader preferably. If  
 127 not displayed, you can find the same animation at the following address: <https://ragonthea.wordpress.com/re->  
 128 [search/fault\\_geom/](#)



129 **Figure S15.** Comparison between two POSTpref models. The coseismic slip is well constrained and do not  
 130 vary between the median model (left) and the maximum a posteriori (right, mode of the gaussian posterior  
 131 distributions of inferred samples) model: the 50 cm contours are shown in black lines. In contrast, the posterior  
 132 uncertainty of the post-seismic slip is large at depth, and median model (left) differs largely from the maximum  
 133 a posteriori model (right). The most probable post-seismic slip area are the ones imaged by the model to the  
 134 right, as shared by most inferred samples. The area of large slip as imaged by the median model and with a  
 135 small posterior uncertainty are also as probable.



136 **Figure S16.** Fit to the InSAR dataset for the median COpref and POSTpref models. Observations, predictions  
 137 inferred from the average model and residuals are shown for ENVISAT descending and COSMO-SkyMed  
 138 ascending interferograms, respectively to the left and to the right. The assumed fault trace is shown with a  
 139 dotted black line. The epicenter is the white star. Seismogenic faults are shown in light gray.



140 **Figure S17.** Cumulative number of events versus time for 6 days after the mainshock (left)  
 141 or the year 2009 (right). The magnitude of completeness is of 0.88 [Valoroso *et al.*, 2013]. The increase around 80 days  
 142 corresponds to the nucleation of several earthquakes of  $M_w \approx 4$  [ChiaraLuce *et al.*, 2011].